ICNMM2009-82010

MODELING AND SIMULATION OF A ROLLERBALL MICROFLUIDIC DEVICE

Luis R. Rojas-Solórzano
Dept. of Energy Conversion
Universidad Simón Bolívar, Venezuela

Shelley L. Anna
Dept. of Mechanical Engineering
Carnegie Mellon University, USA

Bourtal Bradeddine
ETSEIB, EMMME Program
Univ. Politécnica de Catalunya, Spain

Cristina H. Amon
Dept. of Mechanical and Industrial Engineering
University of Toronto, Canada

ABSTRACT

The fluid delivery process through a rollerball device is investigated by means of physical modeling and numerical simulations. The microfluidic device is intended to deliver liquid above a substrate interacting with the surrounding air. While the fluid is delivered, air entrainment occurs through the capillary gap, creating a two-phase liquid-gas mixture whose composition and properties affect significantly the quality of the continuous fluid deposition. For the numerical solution of the 2D two-phase flow governing equations, the finite volume-based finite element method is used with 2nd order time-space schemes for the fully coupled system of equations. The quality of the liquid micro-volume delivery proves to be largely affected by both the speed of the roller and fluid properties. It is found that only under very low speed and some fluid properties, it is possible to guarantee a gas free liquid deposition. Envisioning the potential use of this convenient and popular device in the deployment of microfluid layers or substances at very small quantities with controlled quality, it is apparent the need for handling and channeling out the air entrainment without perturbing the liquid quality.

INTRODUCTION

The rollerball or ballpoint applicator is a device originally conceived in 1888 (Loud, 1888) as a leather marker. However, it was not until 1935 that Frank Klimes and Paul Eisner manufactured and marketed in Prague the first of these instruments, called the Rolpen. Later, in 1943 Laszlo Biro (Biro, 1944) visualized it as a writing instrument with many advantages over the traditional fountain pen. Many things happened since then, as Biro's patent was not originally registered in the USA and in 1945, Milton Reynolds introduced his own version of the device and started successfully commercializing it in the USA. Despite legal disputes, the ballpoint pen business flourished and allowed the appearance of new actors and improvements in the original design and in the formulation of new types of inks. Just to have an idea of this market, according to internet sources (Petrow, A. B., 2009; Russell-Ausley, 2009), more than 2 billion pens are manufactured in the US annually, and the French BIC, for example, manufactures millions of ballpoint pens per day.

The most economical units of ballpoint pens work with oil-based inks in the form of a thick paste. Late and more expensive ballpoints are being manufactured with new formulations of gel-based ink that allow ballpoint pens to perform more like fountain pens. Typical ballpoint pen inks are medium-viscosity, semi-Newtonian, slow drying and free-of-particle fluids intended to allow a continuous paper feed without clogging. Rheology of these inks exhibits modest shear-thinning which prevents their leakage through the openings around the ball when the device is at rest. On the other hand, roller ball pen inks (as compared to ballpoint pen inks), are mostly water-based inks. Water-based inks dry mainly by evaporation and quick wetting of cellulosic fibers in paper substrates (Othmer and Kirk, 2005).

Many inks are characterized by a viscosity of $10 - 20$ Pa.s and a surface tension of 40 mN/m at 20 °C. In the case of the Space Pen, which is pressurized, the ink must be extremely viscous, around $100 - 150$ Pa.s, to prevent it from flowing out under normal rest conditions (Bohnet et al., 2005).

When observing the ballpoint system as a microfluidic device, with the potential of usage for delivering controlled quantities of fluids for different purposes (e.g., medicine, micro-tissues, etc.), it is necessary to inquire how well the device performs. For example: does it ingest air, while discharging liquids as a result of the same roller shearing action? If it does, how much air is entrained into the ink deposit and how does it affect the overall reliability of the instrument? Doesn't it have to deal with the sometimes-questioned quality of writing in ballpoint instruments? For example, even in the newer gel-based (water based) inks, customers (and manufacturers) recognize a good deal of skipping and scratchiness in pen performance that need to be improved (e.g., see Sanford, 2009).

In order to answer these questions and to improve understanding of the operation of this microdevice, this work presents results of 2-D simulations of the operation of a ballpoint pen microfluidic device, based on Newtonian fluids. Results are intended to be of relevance in future microfluidic applications.

NOMENCLATURE

B : body force per unit volume, N/m^3

Bo : Bond number

Ca : Capillary number

d : ¨depth¨ of the 2D-domain, m

$F_{buoyant}$: buoyant force per unit volume, N/m^3

F_{cent} : centrifugal force per unit volume, N/m^3

F_g : gravitational force per unit volume, N/m^3

Fr : Froude number

F_v : viscous force per unit volume, N/m^3

F_γ : surface tension per unit volume, N/m^3

g : gravity acceleration, m/s^2

L : height of the liquid column, m

p : pressure, Pa

P1 : performance coefficient No.1

P2 : performance coefficient No.2

R : disk radius, m

Re : Reynolds number

Ri : Richardson number

$r_{\alpha\beta}$: volume fraction of phases α,β

t : socket radial gap, m

U : fluid velocity, m/s

v : tangential velocity of the disk, m/s

Greek symbols

α,β : subscripts for gas and liquid phases

ρ : density, kg/m^3

κ : curvature, m

μ : dynamic viscosity, Pa.s

θ : contact angle, degrees

γ : surface tension, N/m

ω : angular velocity, rad/s

1. DESCRIPTION OF THE ROLLERBALL MECHANISM

The ballpoint pen has a tiny rollerball made of brass, steel or tungsten carbide at the delivering tip. A liquid reservoir is connected to the rollerball mechanism through a narrow tube (see Fig. 1). The ball, allocated within a socket, rolls as it is dragged upon the surface and delivers the fluid onto it.

A set of some of the most popular over the counter ballpoint oil-based pens were selected, and, through laboratory analysis of the actual dimensions of the mechanism it was verified that dimensions matched quite well the Fisher Space Pen data given in U.S. Patent No. 3.285.228. Therefore, these dimensions were considered for the numerical simulations here performed.
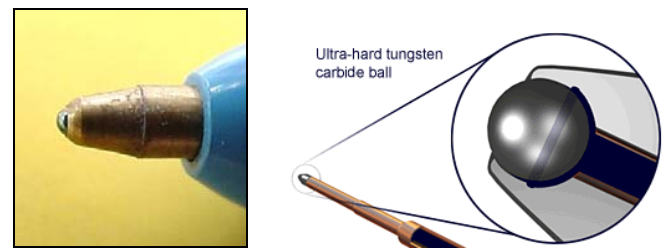

Figure 1: Ballpoint external picture and internal sketch (Russell-Ausley, 2009; Fisher, 2009)

Ballpoint 2D-Model. For the numerical study, the tip geometry (ball and socket) is considered as a 2-D disk-socket array attached to an upper feeding 10-cm liquid column (see Fig. 2).
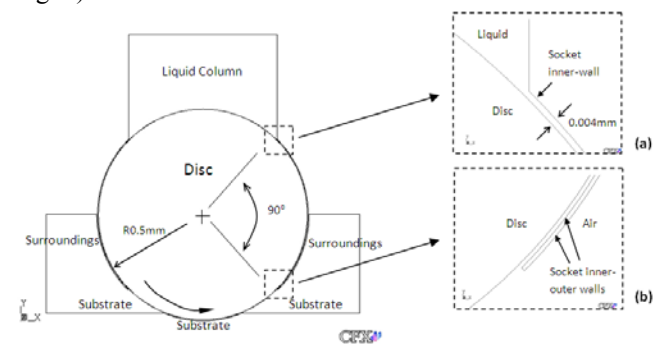

Figure 2: Ballpoint (2D-disk) model. Details at: (a) upper-socket; (b) lower-socket

Ballpoint Dynamics. The forces involved in the operation of the ballpoint might be accounted as: centrifugal force, gravity on the liquid phase, buoyancy on the gas phase, gas-

liquid surface tension, liquid-solid surface tension (by surface wettability), viscous forces (mostly driven by the liquid phase dragged through the gap), and the drag force of the liquid phase against the motion of bubbles. Next, the forces and parameters are presented.

(a) *centrifugal force.* A large centrifugal force would tend to expel the liquid layer away from the disk, diminishing the carrying capacity. The centrifugal force per unit volume on the liquid is computed as:

$$\ddot{F}_{cent} = \rho_{liq} . \frac{V_{\tan g}^2}{R} = \rho_{liq} . \omega^2 . R \tag{1}$$

(b) *gravity force.* Gravity is a driving force pushing the fluid toward the tip and, per unit volume, it is given by:

$$\ddot{F}_{cent} = \rho_{liq} . g \tag{2}$$

(c) *buoyancy force.* The density difference between the two phases may exert a very important buoyant force onto the air entrained into the liquid chamber. The larger the density difference is, the larger the force pulling the air gusts up, toward the top of the liquid tank. This buoyant force per unit volume is computed as:

$$\ddot{F}_{buoyant} = \left(\rho_{liq} - \rho_{air} \right) g \tag{3}$$

(d) *gas-liquid surface tension.* The surface tension accounts for the curvature of the liquid-air interface and the pressure field across the interface as the liquid flows around the wheel and as the air gusts travel within the liquid continuum. In this study, both the wheel and the socket internal walls have been assumed as non-wettable surfaces, while the rest of the walls (ground, tank and socket exterior), have been assumed as wettable surfaces. The net surface force per unit volume originated on the surface tension and angle of contact, will be:

$$\ddot{F}_\gamma = \frac{\gamma 2. (2d + 2t)}{2.R.d.L} \sin(\theta^o) \tag{4}$$

where d, the depth of the quasi-two-dimensional model (i.e., there is no true two-dimensional problem in finite volume) is 4 μm; t is the gap radial clearance of 4 μm; and L is the length of the liquid column being held by the surface tension force, which is approximately 0.1m. Therefore, since d ≈ t, the resulting surface force per unit volume is reduced to:

$$\ddot{F}_\gamma = \frac{\gamma 4}{R.L} \sin(\theta^o) \tag{5}$$

(e) *viscous force.* The viscous force measures the resistance of the bulk flow to be dragged by the shear originated on the roller disk. This force is negligible on the air, but on the liquid, the viscous force per unit volume can be computed as:

$$\ddot{F}_{v\_liq} = \frac{\mu_{liq} . \omega . R}{t^2} \tag{6}$$

(f) *mass flow through the ballpoint.* Similarly, when accounting for the liquid or air mass flow, it is important to compare it against a sensible quantity, which in this case will be taken as the analytical Couette mean flow through the roller-socket gap, called hereafter the ideal flow and given for both phases as:

$$\dot{m}_{ideal\_air/liq} = \frac{\rho_{air/liq} . \omega . R . t^2}{2} \tag{7}$$

(g) *Reynolds number:*

$$Re = \frac{\text{centrifugal force}}{\text{viscous force}} = \frac{\rho_{liq} . \omega^2 . R . t^2}{\mu_{liq} . \omega . R} = \frac{\rho_{liq} . \omega . t^2}{\mu_{liq}} \tag{8}$$

(h) *Froude number:*

$$Fr = \frac{\text{centrifugal force}}{\text{buoyancy on air}} = \frac{\rho_{liq}}{\left(\rho_{liq} - \rho_{air} \right)} \frac{\omega^2 . R}{g} \tag{9}$$

The Froude number measures the tendency of the entrained air to be trapped or to be released toward the top of the tank. The larger the centrifugal force is, the larger the drag of the air around the roller will be and therefore, the more difficult it will be to release or separate it from the dispensed liquid. The opposite occurs for buoyancy. Therefore, a large Fr will promote the air-liquid mixing through the dispenser gap. It is expected that there will be a limiting Fr value as the velocity of the wheel is increased looking for a large rate of liquid outcome.

(i) *Capillary number:*

$$Ca = \frac{\text{viscous force}}{\text{gas - liquid surface tension}} = \frac{\mu_{liq} . \omega . R . R . L}{t^2 . 4 . \gamma . \sin(120^\circ)} = \frac{\mu_{liq} . \omega . R^2 . L}{4 . \gamma . t^2 . \sin(120^\circ)} \tag{10}$$

The Capillary number should capture part of the deviation from the Couette flow as the capillary force together with the pressure affects the pure shear flow. In this case, this number measures the absolute tendency for air entrainment. A large Ca will promote bags of air into the liquid chamber and eventually (depending on the Fr) will permit the air mixing and transport along with the dispensed liquid. On the other hand, a too small Ca will work in the opposite direction.

(j) *Richardson number:*

$$Ri = \frac{\text{gravity}}{\text{inertia}} = \frac{g.d}{(\omega^2 R^2)} \tag{11}$$

(k) *Bond number:*

$$Bo = \frac{\text{gravitational force}}{\text{gas - liquid surface tension}} = \frac{\left(\rho_{liq} - \rho_{air} \right) g . R . L}{4 . \gamma . \sin(\theta^\circ)} \tag{12}$$

(l) *mass ratio:*

$$\dot{m}_{air/liq} \Big/ \dot{m}_{Couette} = M_{air/liq} = \frac{\dot{m}_{air/liq}}{\frac{1}{2} \rho_{air/liq} . \omega . R . t^2} \tag{13}$$

The mass ratio coefficient ($M_{air/liq}$) measures the effective mass of liquid or air that is being pulled into the roller, compared to the amount that should pass in the event of a pure Couette flow situation.

Back of the Envelope Analysis. For a back-of-the-envelope preliminary dynamics analysis, let´s figure the ratio of the inventory forces per unit area, assuming:

R: Tip radius (0.5 mm = 500 μm)

d ≈ t : Socket-ball radial gap (4 μm)

h : Liquid column height (10cm = 0.1m)

Then, by simple observation (using ρ_l =1000 kg/m^3; 10 Pa.s; 10 rad/s; 0.04N/m):

(i)   centrif. force O(10^{-4}) N/m^3 << gravity O(10^{-2}) N/m^3

Thus, centrifugal force is negligible compared to gravity.

(ii) buoyancy on entrained air ~ O(10^{-2}) N/m^3

(iii) surface tension ~ O(10^4) N/m^3

(iv) viscous force ~ [O(10^4)] N/m^3

(v) inertia ~ [O(10^{-2})] N/m^3

(vi) pressure column ~ [O(10^3)] N/m^3

Therefore, it is expected that surface tension, viscous force and pressure column will define the macroscale phenomenon within the ballpoint mechanism. However, gravity and inertia may be comparable to each other and their ratio, i.e., the Richardson number, might augment the intensity of the mixing (Ri<0.25 favors Rayleigh instabilities in stratified flow).

2.   CFD ANALYSIS

A CFD study involves a series of preliminary steps: (a) choosing appropriate governing equations and physical models; (b) discretization of the computational domain and governing equations; (c) setting up boundary and initial conditions; (d) choosing appropriate numerical solver for the set of discretized differential equations; (e) performing mesh and time-step dependency analysis; (f) evaluation of the validity of physical models; (g) finding an approximate solution with a low convergence error; and (h) analysis of results and reassessing of conditions as needed.

The evaluation of the validity of the physical models requires either: (a) to perform key experiments to compare with the numerical results; or (b) to use the analytical solution for a classical problem to compare with the numerical output of the model under physical circumstances similar to the practical problem being assessed. Many authors have already demonstrated how useful and accurate, compared to experimental data, CFD may be in microfluidic analyses (e.g., Schönfeld and Hardt, 2004; Glatzel et al., 2008). In this work, the latter approach was taken, and therefore, it will be presented before the discussion of the boundary conditions taken for the 2D-roller disk.

2.1. Governing Equations and Physical Models

To model the gas-liquid segregated flow, an Eulerian-Eulerian Volume of Fluid (VOF) approach is used for both phases. The mass conservation for each phase and the volume-fraction weighted Navier-Stokes equations of the mixture add to the set of governing equations to be solved. Each phase is considered as an inter-penetrating continuum and both phases are allowed to be present in every point of the domain, just limited by intrinsic volumetric forces (e.g., gravity, centrifugation, etc.), which may tend to segregate them. An interphase sharpening algorithm is enforced and surface tension effects are taken into account by using a discrete approximation of the Young-Laplace equation. Finally, a closure equation is included for the volume fraction, which states that both phases volume fraction must add up to unity at every fluid location.

Therefore, the governing equations are presented, indicating with the sub-index each phase, as follows:

Mass Conservation:
$$\nabla \bullet \left(r_\alpha \rho_\alpha U_\alpha \right) = 0 \tag{14}$$

Linear Momentum:
$$\frac{\partial}{\partial t}(\rho U) + \nabla \bullet \left(\left(\rho U \otimes U - \mu \left(\nabla U + (\nabla U)^T \right) \right) \right) = (B - \nabla p) \tag{15}$$

Furthermore, in this equation:
$$U_\alpha = U_\beta = U \tag{16}$$

$$p_\alpha = p_\beta = p \tag{17}$$

$$\rho = \sum_{\alpha=1}^{2} r_\alpha \rho_\alpha \tag{18}$$

$$\mu = \sum_{\alpha=1}^{Np} r_\alpha \mu_\alpha \tag{19}$$

And the closure for the volume fractions:
$$\sum_{\alpha=1}^{2} r_\alpha = 1 \tag{20}$$

Interphase Refinement Algorithm. The interphase is defined as the surface in which volume fraction for both fluids, r_1 and r_2, are equal to 0.5 each. Firstly, the algorithm identifies the control volumes at the interphase, by checking whether or not r_1-0.5 for certain control volume changes sign with respect to its neighbors. Then, the program identifies the fluid on the wrong side of the interphase and translates it to the right side, ensuring the volume conservation. This surface contouring algorithm requires a local fine mesh.

Surface Tension Model. This model enforces a body force $\vec{F}_S$ on the momentum equation but only for the two or three elements within the smeared interface. The force is calculated as an adaption of the Young-Laplace equation including tangential stresses, which applies on the interface as:
$$\vec{f}_S = \gamma \kappa + \nabla_S \gamma \tag{21}$$

And then reformulated as a continuum force per unit volume (Brackbill et al., 1992) given by:
$$\vec{F}_S = \vec{f}_S \delta_S = \vec{f}_S \left| \nabla r_\alpha \right| = \gamma \kappa \nabla r_\alpha + \nabla_S \gamma \tag{22}$$

In this case, $\nabla_s \gamma$ is zero (e.g., Marangoni stresses are not considered).

While r_α is the volume fraction of the continuous phase (liquid) and the curvature κ is obtained from:

$$\kappa = -(\nabla . \hat{n}) = -\nabla\left(\frac{\nabla r_\alpha}{|\nabla r_\alpha|}\right) \quad (23)$$

The equilibrium contact angle, θ_{eq}, is specified at the free surface interface in contact with a rigid wall in equilibrium. This angle is introduced into the model and it is supposed to be the static contact angle, experimentally measured when the fluid is at rest. The θ_{eq} determines the normal $\hat{n}_{int\_wall}$ to the interface at points $\vec{x}_w$ of contact with the wall as (Brackbill et al., 1992):

$$\hat{n}_{int\_wall}(\vec{x}_w) = \hat{n}_{wall}(\vec{x}_w)\cos(\theta_{eq}) + \hat{n}_t(\vec{x}_w)\sin(\theta_{eq}) \quad (24)$$

where $\hat{n}_t$ lies in the wall and is normal to the contact line between the free surface and the wall at $\vec{x}_w$, and $\hat{n}_{wall}$ is the unit wall normal directed into the wall. The normal $\hat{n}_t$ is calculated as:

$$\hat{n}_t(\vec{x}_w) = \nabla r_\alpha \quad (25)$$

The flow field simulations were performed using ANSYS-CFX. This code is based on the finite volume-based finite element method using a coupled multigrid solver, which solves the full hydrodynamic system of equations simultaneously across all grid nodes.

2.2. Domain and Equations Discretization

The physical domain may be discretized with a mesh of hexahedral, tetrahedral- and/or prism-type finite elements (FE) on which finite sub-control volume domains are defined as shown in Fig. 3 (Burns, 2003):
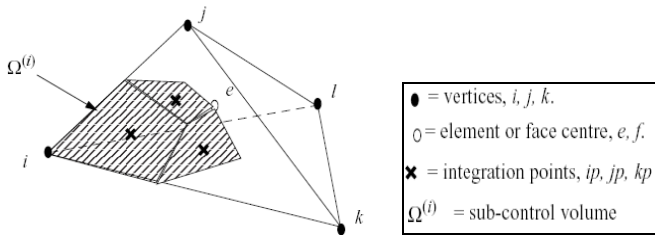
Figure 3: Tetrahedral FE/Hexahedral Sub-control Volume

The finite elements are sub-divided into sub-control volumes, one for each element vertex, by joining the element centroid up to the centroids of the element faces (Burns, 2003). Then, when all macro-elements are assembled, the final control volumes are constructed around common vertices as unions of sub-control volumes, as shown in Fig. 4, for the base of 4 contiguous tetrahedral.

The set of governing equations are integrated over each control volume, such that the relevant quantity (mass and momentum) is conserved for each control volume.
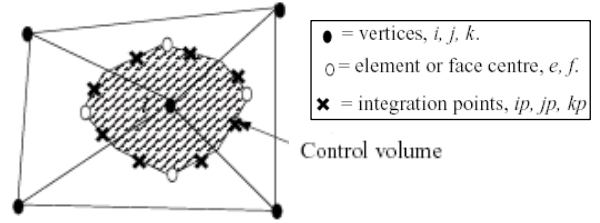
Figure 4: Base surface of Control Volume, constructed out of 4 sub-control volumes

The surface integrals of the conservation equations are calculated by evaluating the variables at the integration points (centroids of sub-control volume faces); then, the discretized equations are assembled by performing volume and surface integrals using an element-by-element procedure. Only the integral points in the interior of the element-to-element set are required for the assembly of the whole set of governing equations. The integration points on the global element boundaries are required for the boundary conditions.

Finally, all the solution variables and physical properties are stored on the FE vertices with a distribution given by local linear shape functions (as for FE).

ANSYS-CFX uses a coupled solver, which solves the governing equations as a single system. This solution approach uses a fully implicit discretization of the equations at any given time step. Initially, the nonlinear system of equations is linearized and then assembled into the solution matrix, which is solved using a Multigrid (MG) accelerated Incomplete Lower-Upper (ILU) iterative method until convergence is reached at the desired level.

The treatment of the governing equations starts from the integration of the set of differential equations using the Gauss' divergence theorem to convert volume integrals into surface integrals (see ANSYS-CFX User's Manual) such that the advection, diffusion and pressure gradient terms remain as fluxes through the control volume faces. The time-discretization of the equations is accomplished using a second-order implicit Euler-Backward scheme. The pressure and velocity are solved in an unstaggered, collocated grid, using the Rhie-Chow algorithm (ANSYS-CFX User's Manual) to overcome the check-board oscillations typical in collocated pressure-velocity grids. The advection term is treated with a high-resolution (second-order) Upwind scheme as proposed by Barth and Jesperson (1989). Further details on the numerical treatment of the equations may be found in ANSYS-CFX User's Manual.

2.3. Validation of Physical Models

It is very important to validate the potential inaccuracy of a solver code before performing massive simulations in particular

types of problem with special physical challenges. For this purpose, even though ANSYS-CFX is a commercial code widely validated, a specific numerical validation of the solver to challenge its capability of modeling interphase phenomena is here presented. The classical capillary rise problem with Rayleigh's analytical solution was chosen as benchmark.

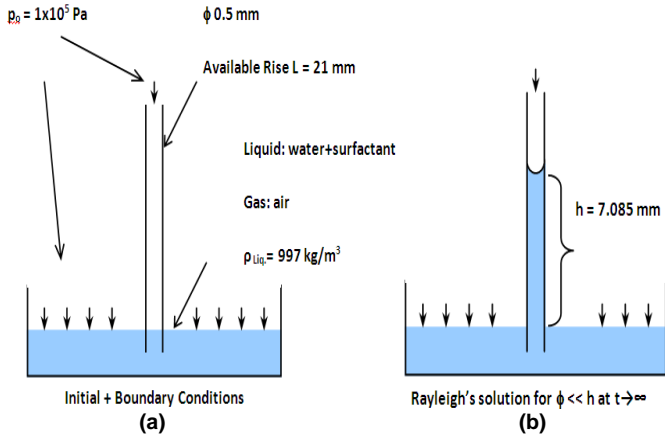Figure 5 shows the set up of the physical problem, as well as the analytical solution of Rayleigh.

Figure 5: Capillary rise phenomenon: a) Initial-Boundary Conditions; b) Rayleigh's solution at equilibrium

The numerical simulation was performed on a ¼ of the geometry by taking advantage of symmetry in the actual domain. The runs were executed on a PC using an Intel Core 2 Duo T7200 2.0GHz processor, with 2GB-Ram. The strategy to converge the final solution was based on using a coarse mesh for the whole domain except for the region of the meniscus (rounding 100.000 macro-elements with 5 layers of prisms along the walls, 8-9 tetrahedra layers along the meniscus radius and 0.7 mm average-element everywhere else), for the first time-steps; then, re-meshing after rising the meniscus every 1 mm approximately, moving the denser grid towards the new meniscus path (keeping the same density as before). Previous mesh data were interpolated into the newer mesh to restart the new 'rise-step' simulation, and so forth. This primary worm-like meshing procedure ended with Mesh 1, after which, a secondary, more sophisticated procedure, described below, took place. The rise of the meniscus occurred asymptotically, rising very fast at the very beginning until it reached the first 0.01s; from this time, it dramatically slowed down (see Fig. 6). This almost monotonic rise, although aimed to the right position, didn't reflect important oscillations, previously observed around the final position (Zhmud et al., 2000; Quinte et al., 2001), probably because of a series of factors: a) worm-like mesh strategy may have caused large dissipation through the domain; and b) using a static contact angle throughout the whole simulation surely affected the transient results.

Once the meniscus reached the quasi-equilibrium position, then a new re-meshing procedure started: (a) Mesh 2: firstly the Mesh 1 was coarsened out evenly and then refined strictly only at the meniscus location and along the free surface of the vessel to capture the static reservoir around the capillary. Thus, Mesh 2 used the same density at the meniscus as the previous Mesh 1, while a 0.2 mm average-element was used for the vessel free surface and 0.7 mm everywhere else; (b) Mesh 3: a second refinement, now onto Mesh 2, of about a half the size of the mesh, just on the meniscus, was performed. Results from (a) and (b) were compared with a mean height difference smaller than 0.25 % showing mesh independence of the results. The time-step was adjusted in such a way that convergence was fulfilled before 10 iterations with residuals of the governing equations forced to be less than 0.01% of the normalized leading term.
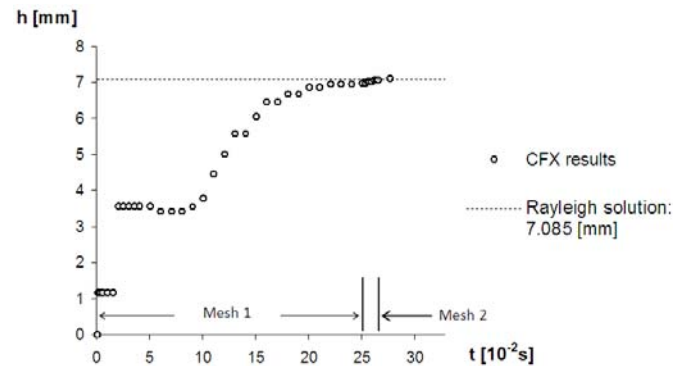

Figure 6: Rise of the meniscus vs. time. Results from simulation and Rayleigh's solution

Table 1 shows computational data for the mesh just when the meniscus reached the top position (mesh 1), and for the two more refinements (meshes 2 and 3) to give an idea of the CPU-time and memory demand of the problem. The results at different times for mesh 2 are shown in Fig. 7. The equilibrium height for mesh 2 was determined for the moment at which the solution changed less than 0.5% within an interval of 0.01s. The solution for mesh 3 was obtained after re-starting from the solution for mesh 2.

Table 1: Computational demand and numerical-analytical differences for Capillary Rise validation

Mesh	Elements	Time-step [s]	Memory Used [MB]	h_{num} [mm]	$\dfrac{(h_{Rayleigh} - h_{num})}{h_{Rayleigh}} \times 100\%$
1	104.264	0.0001	~150	7.021	0.9%
2	199.276	0.0001	~204	7.111	0.37%
3	213.632	0.0001	~220	7.126	0.58%

The final CFD asymptotic value deviates from Rayleigh's solution by less than 1%.

Figure 7: Numerical results. Free surface in actual 3D simulation geometry at: (a) t=0s; (b) t=0.05s; (c) t=0.2763s (equilibrium time); and 2D views at: (d) t=0s; (e) t=0.05s; (f) t=0.2763s (equilibrium time)

2.4 CFD Analysis of the Ballpoint Device

This section is divided into: (a) setting-up boundary conditions and domain meshing; (b) mesh-independence assessment; (c) description of physical parameters of interest; and (d) analysis of results.

Boundary Conditions and Computational Mesh. Figure 8 shows the boundary conditions adopted for the 2D-simulation. A unit-depth hexahedron-based mesh was chosen. Meshes with 78000(XX-Coarse), 98000(Coarse), 188000(Medium) and 350000(Fine) nodes were preliminarily evaluated to assess the mesh dependency. Aiming to a well-solved boundary layer flow within the wheel-socket gap, all meshes were provided with approximately 12 elements across the socket-disk gap, while more or less dense meshes were placed everywhere else. Details of the Medium mesh (188k nodes) are shown in Fig. 9.

Figure 8: Boundary Conditions (a) detail upper-socket; (b) detail lower-socket. (*) + developed flow: $\partial \vec{u} / \partial n = 0$

Figure 9: Meshing details (a) detail upper-socket; (b) detail lower-socket

The strategy to perform the simulations was as follows: (a) starting from initial conditions of liquid at rest above the disk, and air at rest underneath, a transient simulation with t-steps of 0.1s was performed to advance toward the quasi-steady solution; (b) then, the simulation was re-started, using t-steps of 0.0001s, in order to stabilize the simulation to obtain the quasi-steady solution. The mass ratio coefficient ($M_{air/liq}$) is used for checking the correct convergence of the steady simulations, as the mass flow balance for the whole domain should result in less than 1% of the Couette equivalent mass flow, to consider the case to be converged.

For the simulations, liquid properties were varied according to some authors (Othmer and Kirk, 2005) references on oil-based inks, which typically have viscosities of $\mu \sim 10 - 20$ Pa.s (10.000 cP – 20.000 cP), and surface tension with air of $\gamma \sim 0.04$ N/m. Tests run at Dr. Shelley Anna´s Laboratory with a sample of commercial ballpoint pens led to an average density of $\rho \sim 1200$ kg/m^3 for the oil-based inks. However, these figures are for reference purposes only, since this study aims to project the ballpoint pen device beyond the mere writing instrument. Table 2 presents the range of meshes and physical parameters explored in this investigation.

Table 2: Physical Parameters for Ballpoint Simulations

Property	Values
Mesh coarseness	XX Coarse 78k - Coarse 98k - Med 188k - Fine 350k [nodes]
Liquid viscosity, μ_l	1000 – 10000 [cP]
Liquid density, ρ_l	880 – 1200 – 2000 – 4000 [kg/m^3]
Surface tension, γ	0.004 – 0.04 [N/m]
Wheel angular speed, ω	1 – 5 – 10 – 20 [rad/s]
Linear speed, v	0.5 – 2.5 – 5 – 10 [mm/s]
Contact angle (wheel/socket), θ	90 – 120 [degrees]

Mesh Dependency Assessment. The mesh dependency was evaluated by choosing an average case and evaluating the fluid velocity profile at the mid angle of the left socket. Figure 10 depicts the comparison and it is clear the difference between xx-coarse and coarse meshes vs. medium and fine meshes. For an economical and accurate solution, the medium mesh is sufficient. Therefore, this is the mesh used thereafter in the CFD analysis.

Effect of the Liquid Viscosity. Figures 11 and 12 show that a larger liquid viscosity increases the amount of liquid transported by the disk. For the 10 times larger liquid viscosity, a 15% larger liquid presence is observed within a 1μm strip above the disk. For both viscosities, the entrained gas is partially transported, while creating a bubble-like structure on the left-upper entrance of the socket gap. Also, for the larger viscosity, this bubble-like structure relaxes towards the top of the liquid reservoir (see Fig. 11-A). However, no change is noticed in the velocity profile of the mixture within the gap.

Effect of the Liquid Density. The influence of the density is not significant, as shown in Figs. 13 and 14. The larger density promotes about 5% more liquid within the strip closer

to the disk, while the opposite occurs within the strip closer to the wall.
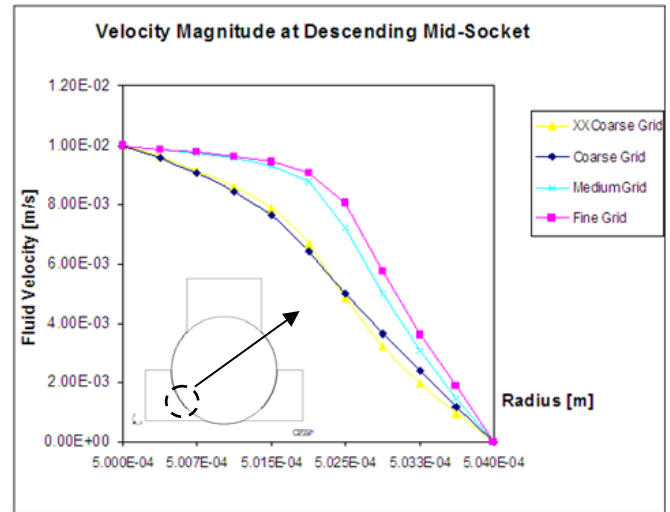
$$\mu_l = 10000 \text{ cP}, \varrho_l = 1200 \text{ kg/m}^3, \gamma = 0.04 \text{ N/m},$$
$$\omega = 20 \text{ rad/s}, v = 5 \text{ mm/s}, \theta = 90 \text{ deg}$$

Figure 10: Comparison of fluid velocity at mid-angle of left side socket-disk gap, for different meshes.
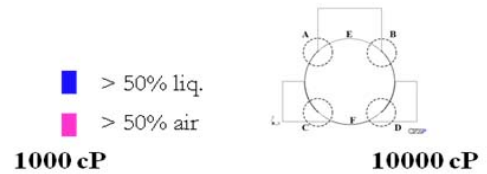
Conditions: $\rho = 1200$ kg/m^3; $\gamma = 0.04$ N/m; $\omega = 20$ rad/s; v = 10 mm/s; $\theta = 90$ deg.

Figure 11: Shaded contours of fluids volume fraction as a result of changing the liquid viscosity.

Effect of the Surface Tension. The surface tension exerts dramatic changes in the phase distribution and liquid transport. A smaller surface tension facilitates the gas entrainment into the liquid column, as seen in Fig. 15-A, while at the same time, favors the liquid transport towards the disk-socket gap. The velocity of the mixture increases up to 30% for the smaller surface tension, while an almost perfect stratification of the

8

phases is appreciated within the gap. Liquid flows preferentially, and almost exclusively, within the half gap closer to the disk, as seen in Fig. 16.
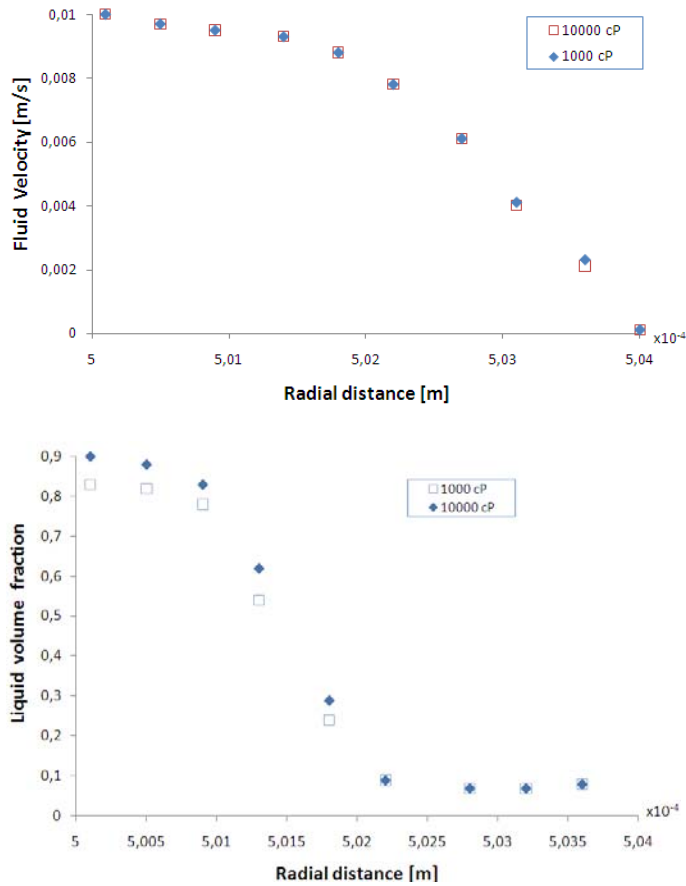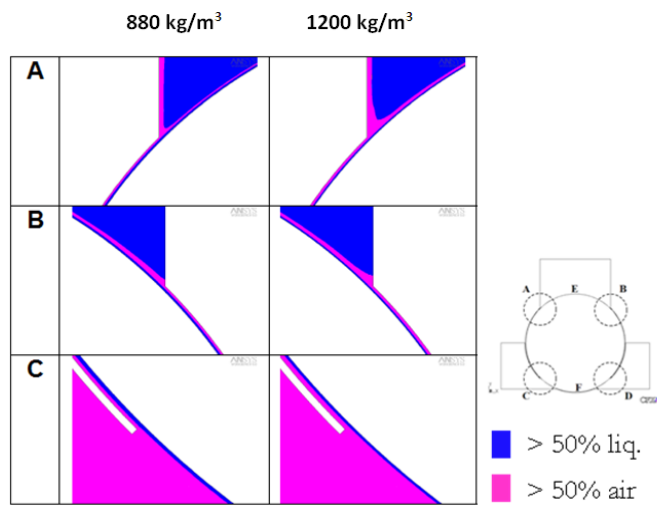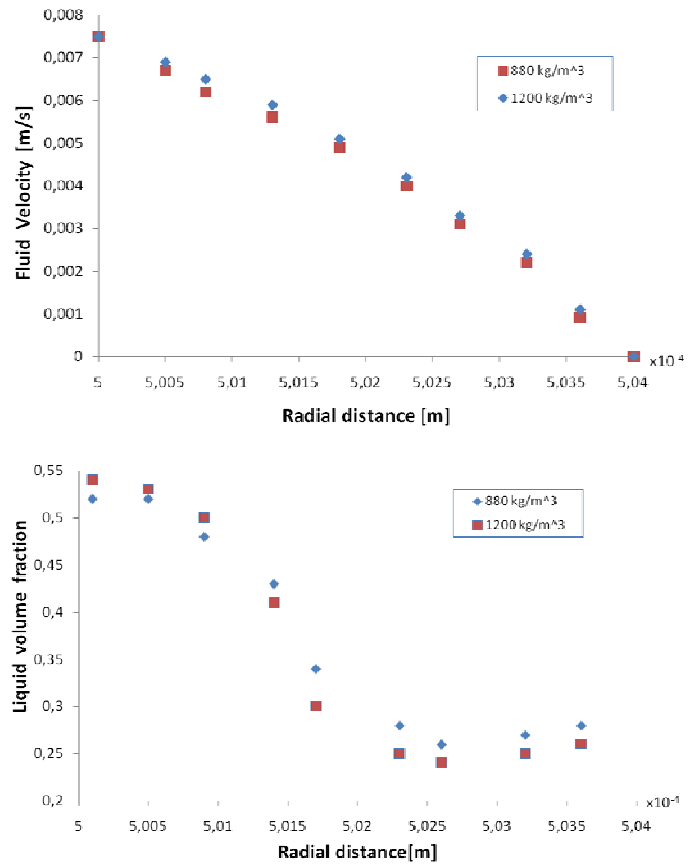

Figure 12: Effect of liquid viscosity on fluid velocity and volume fraction at mid-angle of left side socket-disk gap.

Conditions: $\sigma = 0.04$ N/m, $\mu = 10000$ cP, $\omega = 20$ rad/s, $v = 10$ mm/s, $\theta = 90$ deg.

Figure 13: Shaded contours of fluids volume fraction as a result of changing the liquid density.

Figure 14: Effect of liquid density on fluid velocity and volume fraction at mid-angle of left side socket-disk gap.

Effect of the Surface Tension. The surface tension exerts dramatic changes in the phase distribution and liquid transport. A smaller surface tension facilitates the gas entrainment into the liquid column, as seen in Fig. 15-A, while at the same time, favors the liquid transport towards the disk-socket gap. The velocity of the mixture increases up to 30% for the smaller surface tension, while an almost perfect stratification of the phases is appreciated within the gap. Liquid flows preferentially, and almost exclusively, within the half gap closer to the disk, as seen in Fig. 16.

Effect of the Angular Velocity. While the phase distribution is almost unaltered within the socket-disk channel for different angular velocities (see Fig. 17), the fluid (mixture) velocity, as expected, changes accordingly with the angular velocity, as seen in Fig. 18.

Effect of the Contact Angle. Changes in the contact angle only affect the static condition, while the liquid-solid-gas intersection exists. Therefore, as appreciated in Figs. 19 and 20, this parameter does not exert changes in either the fluid velocity or in the global phase distributions. Just a minor (less than 10%) change in the maximum fluid velocity is observed.
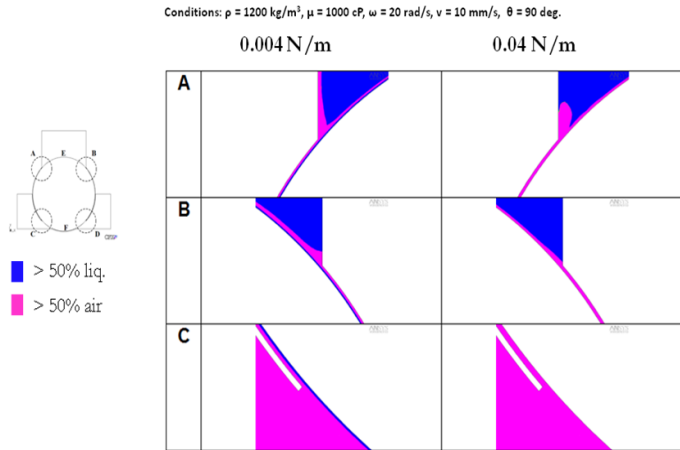
Copyright © 2009 by ASME

Figure 15: Shaded contours of fluid volume fraction as a result of changing the surface tension.
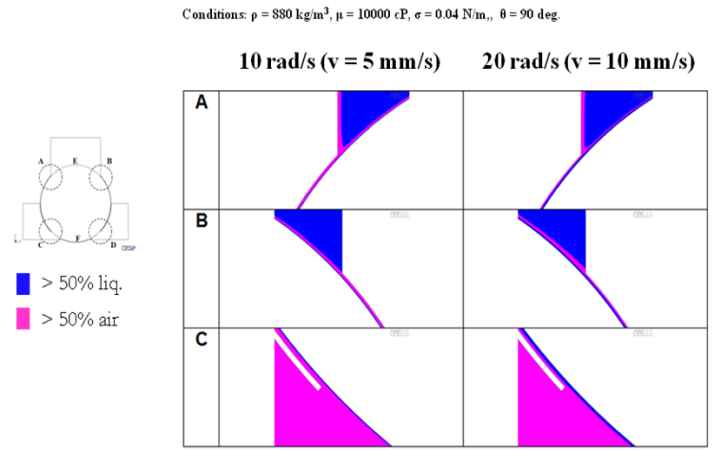

Figure 17: Shaded contours of fluids volume fraction as a result of changing the angular velocity.
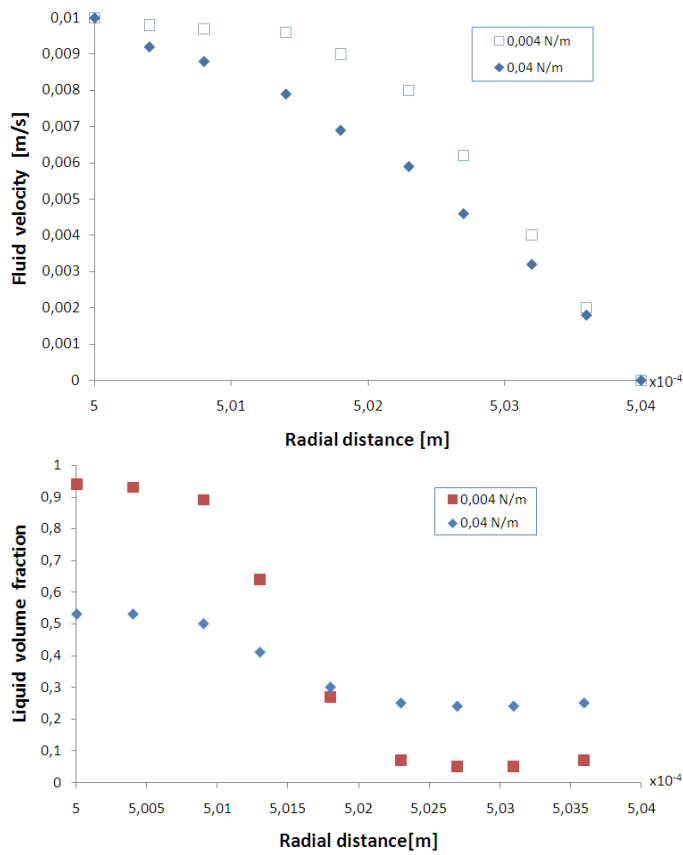

Figure 16: Effect of surface tension on fluid velocity and volume fraction at mid-angle of left side socket-disk gap.
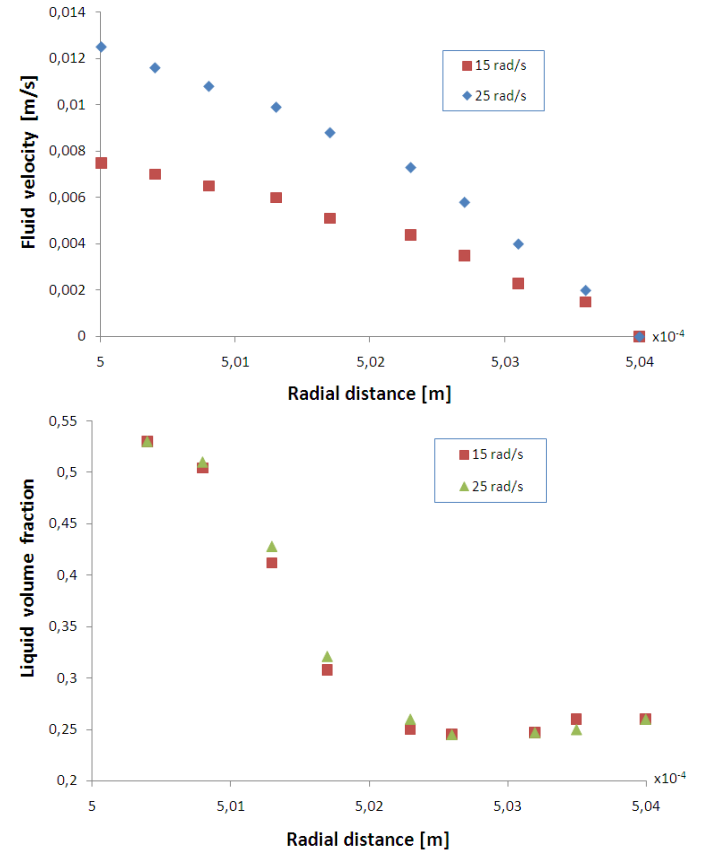

Figure 18: Effect of angular velocity on fluid velocity and volume fraction at mid-angle of left side socket-disk gap.

Conditions: $\rho = 1200$ kg/m^3, $\omega = 20$ rad/s, $v = 10$ mm/s, $\mu = 10000$ cP, $\sigma = 0.04$ N/m.
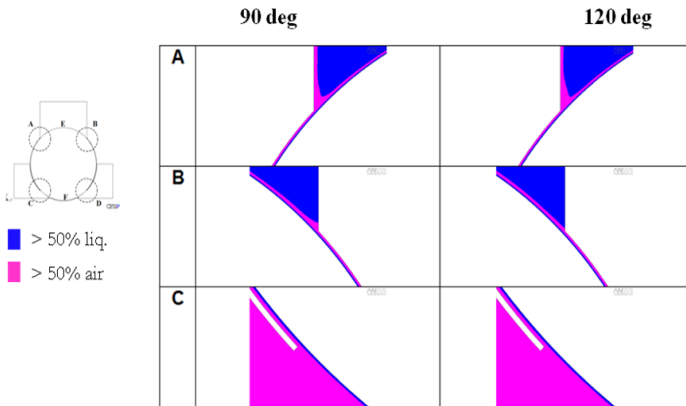
Figure 19: Shaded contours of fluid volume fraction as a result of changing the contact angle.
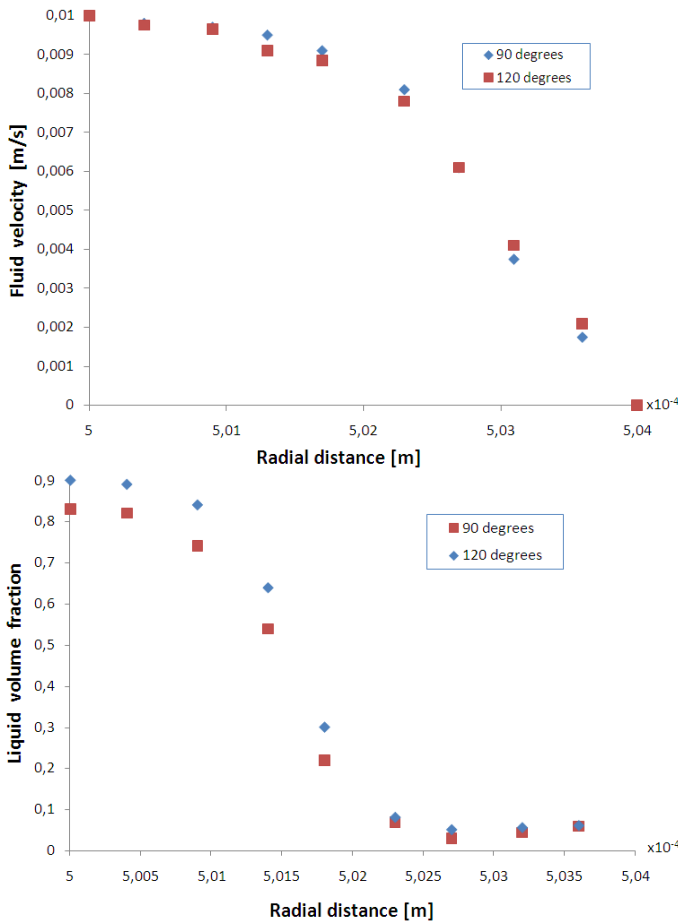

Figure 20: Effect of contact angle on fluid velocity and volume fraction at mid-angle of left side socket-disk gap.

P1 and P2 Performance Parameters. Two performance parameters have been here proposed: P1 and P2. The first one measures the ratio between the actual liquid flow coming out of the device´s socket and the theoretical Couette-Poiseuille liquid flow, while the second one measures the ratio between the actual liquid flow and the total amount of mixture flow coming out of the device. Therefore, P1 refers to how close to a one-phase laminar flow the device performs, while P2 refers to how much gas entrains the delivered liquid. In fact, as shown in Figs. 21 and 22, both parameters, as a function of the Bo and Ca numbers respond likewise. Figures 21 and 22 show that the capillarity markedly affects the performance of the device, by increasing the gas-free delivery as the Ca number increases (larger viscosity and/or smaller surface tension). However, it is not clear yet the influence of the Bo number, for which the P1 and P2 parameters show sensitivity, but without a well defined dependency. Additional numerical tests are ongoing in order to clarify that dependency.
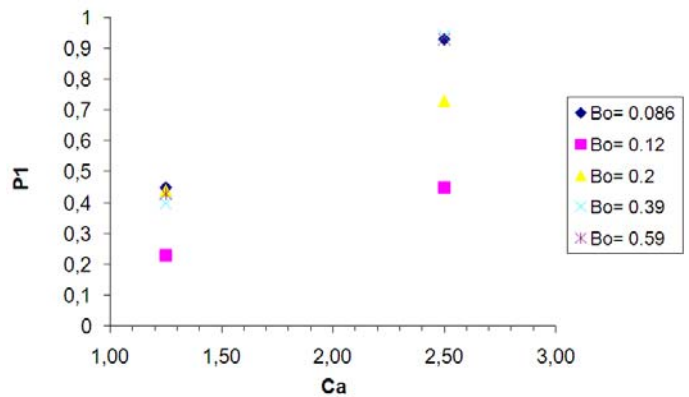

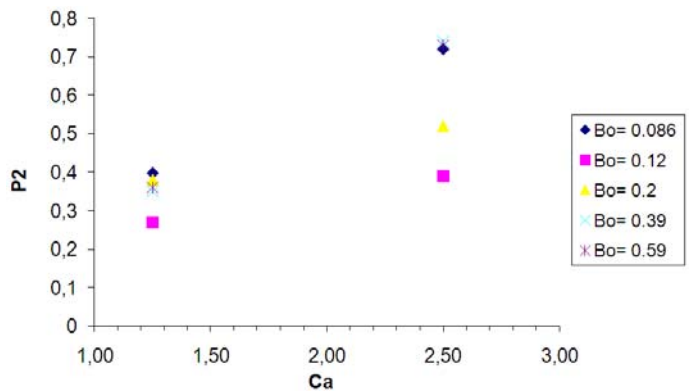**Figure 21:** Performance (P1) of the 2D-microdevice as a function of the Capillary and Bond numbers.

Figure 22: Performance (P2) of the 2D-microdevice as a function of the Capillary and Bond numbers.

CONCLUDING REMARKS

The CFD study of a ballpoint microfluidic delivery mechanism is presented. A 2D-incompressible two-phase model is assumed, considering surface tension and contact angle parameters. The performance of the device is analyzed as a function of relevant physical parameters, including liquid viscosity-density, surface tension, contact angle and angular

velocity. Both viscosity and surface tension proved to be the most relevant parameters influencing the performance of the device, in agreement with the back-of-the-envelope analysis. An almost gas-free operation is only obtained at large Capillary numbers. Therefore, a careful selection or modification of the liquid viscosity and surface tension, according to specific applications, may lead to a promising future for these mechanisms, not only as a much better writing instruments, but also as a novel microfluidic deposition devices. Nevertheless, further analyses must be undertaken in order to detail a performance curve of the device including, for example, 3D effects and compressibility issues.

ACKNOWLEDGMENTS

REFERENCES

1. Adamson, A. and Gast, A., Physical Chemistry of Surfaces, John Wiley & Sons, Inc., 6 ed., 1997.
2. Barth, T. J. and Jesperson, D. C., "The Design and Application of Upwind Schemes on Unstructured Meshes". AIAA Paper 89-0366, 1989.
3. Biro, L., London Patent Office Spec. No. GB-564,172, Sept., 1944.
4. Bohnet, M., et al., Ullmann´s Encyclopedia of Industrial Chemistry, John Wiley & Sons Inc., 2005.
5. Brackbill, J.U., Kothe, D.B. and Zemach, C., "A Continuum Method for Modelling Surface Tension". Journal of Computational Physics, 100:335-354, 1992.
6. Burns, A., Computational Fluid Dynamics Modeling of Multi-Phase Flows, Lecture Notes, Alpha Beta Numerics, 2003.
7. Fisher, ¨Technology¨, Engineered for Better Writing, Fisher Space Pen (Canada), January 9th, 2009, http://www.spacepen.ca/cdn-english/tech_point.htm, 2009.
8. Glatzel, T., Litterst, C., Cupellia, C., Lindemann, T., Moosmann, C., Niekrawietz, R., Streule, W., Zengerle, R. and Koltay P., ¨Computational fluid dynamics(CFD) software tools for microfluidic applications–A case study¨. Computers & Fluids, 37, 218–235, 2008.
9. Loud, J., U.S. Patent No. 392,046, Oct., 1888.
10. Othmer, D. F., and Kirk, R. E., Kirk-Othmer Encyclopedia of Chemical Technology, John Wiley & Sons, Inc., 2005.
11. Petrow, A. B., ¨Pen Facts.¨, Handcrafted Harwoods, Pen History, January 9th, 2009 <http://woodpensonline.com/history.htm>, 2009.
12. Quinte, A., Halstenberg, S., and Eggert, H, "Use of Numerical Methods for Modeling and Simulating Capillary Driven Flows in Microchannels", Technical Proceedings of the 2001 International Conference on Modeling and Simulation of Microsystems, South Carolina, USA, Nanotech 2001, Vol. 1, pp. 250-253, 2001.
13. Russell-Ausley, M., ¨How Ballpoint Pens Work.¨, Howstuffworks?,http://home.howstuffworks.com/pen.htm, 2009.
14. Schönfeld, F. and Hardt S., ¨Simulation of Helical Flows in Microchannels¨. AIChE Journal, Vol. 50, No. 4, 2004.
15. Sanford, ¨Got a question, Need advice, We can help.¨, Consumer Corner, Sanford Brands, Sanford a Newell Rubbermaid Company 2001-2005, January 9th, 2009 http://www.sanfordcorp.com/sanford/consumer/jhtml/help/sanford_help_91.jhtml, 2009.
16. Zhmud, B.V., Tiberg, F., and Hallstensson, K, "Dynamics of Capillary Rise". Journal of Colloid and Interface Science 228, 263-269, 2000.